Nanoscale

Accepted Manuscript

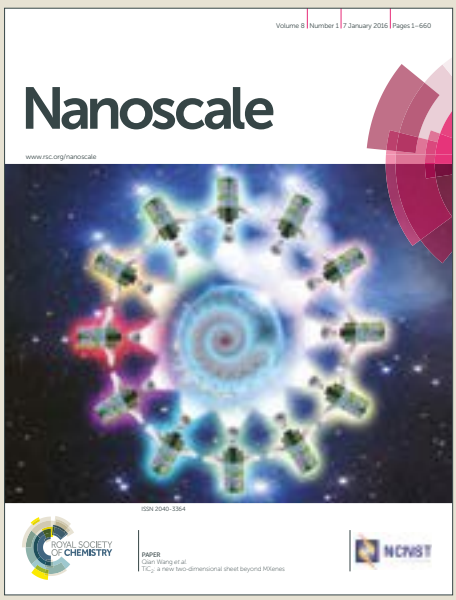

This is an Accepted Manuscript, which has been through the Royal Society of Chemistry peer review process and has been accepted for publication.

Accepted Manuscripts are published online shortly after acceptance, before technical editing, formatting and proof reading. Using this free service, authors can make their results available to the community, in citable form, before we publish the edited article. We will replace this Accepted Manuscript with the edited and formatted Advance Article as soon as it is available.

You can find more information about Accepted Manuscripts in the author guidelines.

Please note that technical editing may introduce minor changes to the text and/or graphics, which may alter content. The journal's standard Terms & Conditions and the ethical guidelines, outlined in our author and reviewer resource centre, still apply. In no event shall the Royal Society of Chemistry be held responsible for any errors or omissions in this Accepted Manuscript or any consequences arising from the use of any information it contains.

ROYAL SOCIETY OF CHEMISTRY

rsc.li/nanoscale

InP-$In_xGa_{1-x}As$ Core-Multi-Shell Nanowire Quantum Wells with Tunable Emission in the 1.3 – 1.55 µm Wavelength Range

H. A. Fonseka,[1a*] A. S. Ameruddin,[1, 2] P. Caroff,[1b*] D. Tedeschi,[3] M. De Luca,[3c] F. Mura,[4] Y. Guo,[1d] M. Lysevych,[5] F. Wang,[1e] H. H. Tan,[1] A. Polimeni,[3] and C. Jagadish[1]

[1]*Department of Electronic Materials Engineering, Research School of Physics and Engineering, The Australian National University, Canberra, ACT 2601, Australia*

[2]*Faculty of Science, Technology and Human Development, Universiti Tun Hussein Onn Malaysia, Parit Raja, 86400, Batu Pahat, Johor, Malaysia*

[3] *Dipartimento di Fisica and CNISM, Sapienza Università di Roma, Piazzale A. Moro 2, 00185 Roma, Italy*

[4] *Dipartimento di Scienze di Base e Applicate per l'Ingegneria, Sapienza Università di Roma, Via Scarpa 16, 00185 Roma, Italy*

[5]*Australian National Fabrication Facility, Research School of Physics and Engineering, The Australian National University, Canberra, ACT 2601, Australia*

Abstract: The usability and tunability of the essential InP-InGaAs material combination in nanowire-based quantum wells (QWs) are assessed. The wurtzite phase core-multi-shell InP-InGaAs-InP nanowire QWs are characterised using cross-section transmission electron microscopy and photoluminescence measurements. The InP-InGaAs direct interface is found to be sharp while the InGaAs-InP inverted interface is more diffused, in agreement with their planar counterpart. Bright emission is observed from the single nanowires containing the QWs at room temperature, with no emission from the InP core or outer barrier. Tunability of the QW emission wavelength in the 1.3 – 1.55 µm communications wavelength range is demonstrated by varying the QW thickness, and in the 1.3 µm range by varying composition. The experiments are supported by simulation of the emission wavelength of the wurtzite phase InP-InGaAs QWs in the thickness range considered. The radial heterostructure is further extended to design multiple QWs with bright emission, therefore establishing

*Correspoding authors: a.fonseka.1@warwick.ac.uk, CaroffP@cardiff.ac.uk

Present addresses:

[a] *Department of Physics, University of Warwick, Coventry CV4 7AL, United Kingdom*

[b] *School of Physics and Astronomy, Queens Building, The Parade, Cardiff, CF24 3AA, United Kingdom*

[c] *Department of Physics, University of Basel, Klingelbergstrasse 82, 4056 Basel, Switzerland*

[d] *Samsung Austin Semiconductors, 12100 Samsung Blvd, Austin, TX 78754, United States*

[e] *Institute for Biomedical Materials and Devices, Faculty of Science, University of Technology Sydney, Sydney, NSW 2007, Australia*

the capability of this material system for nanowire based optical devices for communication applications.

1. Introduction

InP-InGaAs material system is being extensively used in planar optical and electronic devices. There are a number of reasons for the widespread use of this material combination. The ability to achieve perfect lattice matching to well established InP at the composition of 53% In in InGaAs allows easy design of heterostructures by minimising mechanical strain and avoiding critical layer thickness limitation. The possibility to selectively etch one material over the other in a very controlled manner provides a high level of freedom in processing and device fabrication.[1] It has also been shown that the small electron effective mass in InGaAs and the large Γ-L energy spacing of the binary InP lead to high quantum efficiency and responsivity in devices based on quantum well (QW) structures such as infra-red photodetectors, compared to the other popular lattice-matched AlGaAs-GaAs alternative.[2, 3] Most importantly, using this material combination, quantum confined structures such as QWs and dots can be designed and tuned to operate in the 1.3–1.55 μm range, which encompasses the low dispersion and low attenuation wavelength window used in modern optical communication systems.[4] InP-InGaAs multiple quantum well (MQW) modulators,[4] laser diodes,[5] waveguides[6] and photodetectors[7, 8] are some of such essential components used in these communication systems.

Over the past decade, extensive research has been carried out to replicate planar device structures in the nanowire form, with the intention of making use of the inherent advantages of the nanowire geometry in order to improve their performance. Although nanowire heterostructures combining various materials have been extensively reported,[9-20] reports on the use of InP-InGaAs material combination in nanowires have been surprisingly rare.[12, 21-25] In fact, InP-InGaAs nanowire QWs have not been reported despite popularity of their planar counterpart.

Core-shell QWs formed on the nanowire side facets are one of the most effective architectures to make use of the large surface area of the nanowires, creating large active regions without compromising the device footprint. Hence, the present study investigates the use of the mature InP-InGaAs material system in core-shell nanowire QW structures. The $In_xGa_{1-x}As$ QWs are successfully grown around InP nanowires and another InP shell is used as the second barrier. A MQW structure comprised of three QWs is grown by repeating the QW and barrier growth steps. Detailed structural analysis is carried out on the nanowire SQWs using cross-sectional transmission electron microscopy (X-TEM). Micro-photoluminescence (μ-PL) measurements and μ-PL mapping are used for optical characterisation of the single and multiple QWs. The SQW emission is tuned in the optical communications wavelength region of 1.3 – 1.55 μm by varying the well thickness and in the 1.3 μm region by varying its composition. The emission wavelength as a function of the thickness of these

wurtzite (WZ) phase QWs is modelled using the experimental emission wavelength data and single band effective mass approximation.

2. Experimental Methods

The InP-InGaAs nanowire QWs were grown in a horizontal flow metal organic vapour phase epitaxy (MOVPE) reactor with a total flow rate of 15 slm, using trimethylindium (TMIn), trimethylgallium (TMGa), phosphine (PH_3) and arsine (AsH_3) as precursors. Two series of samples were grown on InP (111) B substrates, one with varied QW thicknesses (while maintaining the same composition) and other with varied composition between GaAs and InAs while scaling the growth time to achieve the same nominal thickness of 7 nm. The QW-barrier growth steps were repeated in order to grow the MQW structure. More details on the growth procedure can be found in the Supporting Information, Section 1. The nanowire single quantum well (SQW) grown with In molar fraction (X_v = [TMIn]/([TMIn]+[TMGa])) = 0.55 in the vapour phase and nominal thickness of 7 nm was used as the principal sample for the detailed structural and optical analysis shown in Section 3.1.

Morphological, structural and compositional analysis of the nanowire QWs were carried out using scanning electron microscopy (SEM) and transmission electron microscopy (TEM) – operated in both, conventional and scanning transmission electron microscopy (STEM) modes. Lateral X-TEM samples were prepared by microtome sectioning and all cross–sections analysed were from the 1-2 μm region from the bottom of the nanowires.

The as-grown nanowires were transferred to silicon or sapphire substrates before μ-PL measurements in order to eliminate contribution from the parasitic planar QW that may have simultaneously grown on the substrate. Single nanowire PL was excited using a 633 nm continuous wave HeNe laser with a spot diameter of ~1 μm and excitation power of 20 μW. PL was detected using a nitrogen cooled InGaAs detector. For the μ-PL mapping study, suitable single nanowires were identified by SEM prior to PL measurements. Spectra were obtained by scanning in 300 nm steps along the nanowires at 80 K. The excitation laser wavelength was 532 nm and the spot diameter was ~ 1 μm. The luminescence was spectrally dispersed by a 0.75 m long monochromator equipped with a 300 grooves/mm diffraction grating. The signal was detected by a liquid nitrogen-cooled InGaAs array. At least seven nanowires were measured from each sample for the single nanowire measurements. PL measurements on nanowire ensembles shown in Fig. 4 (c) and (d), were carried out by exciting the samples with a laser diode (λ = 632.8 nm) focused to a spot of ~ 200 μm diameter, chopped at 375 Hz and excitation power of 500 μW. The PL signal was dispersed by 0.25 m focal-length monochromator equipped with a 300 grooves/mm grating and detected by a liquid-nitrogen-cooled InGaAs photodiode coupled to a lock-in amplifier.

3. Results and Discussion

3.1 Single and Multiple Quantum Well Nanowires

Fig. 1 (a) shows an SEM image of the principal sample with nominally 7 nm thick QW of composition X_v = 0.55 and the inset shows the top view with respect to the {110} cleavage plane. The final structure is around 4.2 μm in length and has a predominantly WZ crystal phase with stacking faults and occasional thin zincblende (ZB) insertions (see Fig. S1 in Supporting Information). The InP nanowire core (not shown) has a hexagonal cross-section shape with non-polar {1-100} type side facets. As confirmed by the top view SEM image in Fig. 1 (a), these {1-100} facets remain unchanged during temperature ramp-up and QW growth. A schematic sketch of the structure is shown in Fig. 1 (b). In some nanowires the InP axial segment grown during the InP barrier growth is kinked or irregular as seen in the nanowire indicated by an arrow in Fig. 1 (a).

Cross-sections of the nanowire QWs were analysed in order to gain further understanding of their internal structure. Fig. 1 (c)i-iv show energy dispersive x-ray spectroscopy (EDXS) analysis maps from a cross-section of a nanowire from the nominally 7 nm thick QW sample showing the distribution of each element. The spatial distribution of each element is clear and as expected, demonstrating the formation of InGaAs QW and InP outer barrier on the facets of the InP nanowire core. Quantitative EDXS analysis was carried out on the nanowire cross-sections in order to ascertain the actual $In_xGa_{1-x}As$ composition in the solid phase (x). Due to limited resolution of the STEM probe and to avoid contribution from the InP core and barrier, a much thicker InGaAs shell of 50 nm nominal thickness, grown under identical growth conditions was analysed for this purpose. The In fraction in solid x was found to be 0.600 ± 0.025 creating small lattice mismatches of 0.51% and 0.37% with InP along *a* and *c* axes of the crystal, respectively.[26-28] It should also be noted that alloy segregation seen in the apices and facets of some ternary nanowire structures[9, 12-15, 29, 30] was not observed in this case, at the current InGaAs composition, within the sensitivity of the measurements.

Fig. 1 (d)i shows a high-angle annular dark field (HAADF) STEM image of the same cross-section as in Fig. 1 (c). The QW is visible in lighter contrast compared to the InP core and barrier, due to the sensitivity of the imaging mode to the atomic number, Z. The magnified view from the marked area shown in Fig. 1 (d)ii reveals that the first InP to InGaAs (direct) interface is sharp while the second InGaAs-InP (inverted) interface is diffused compared to the first. As shown in Fig. 1 (d)iii, this can be further confirmed by the rate of change (derivative) of the integrated intensity profile taken from the area marked in yellow in Fig. 1 (d)ii, where it is clearly seen that the FWHM (marked with black arrows) is larger for the inverted interface. Similar difference in sharpness has also been observed in InGaAs-InP QWs grown on planar surfaces.[31-34] Some of the same causes are applicable to QWs grown around nanowires as the growth mechanism is similar (vapour-solid) in both cases despite the differences in facets, crystal phase and structure. Group V interdiffusion[32, 35-37] that takes place as a result of As-P exchange (which is promoted by the stronger chemical bond between Ga and P)[32] and

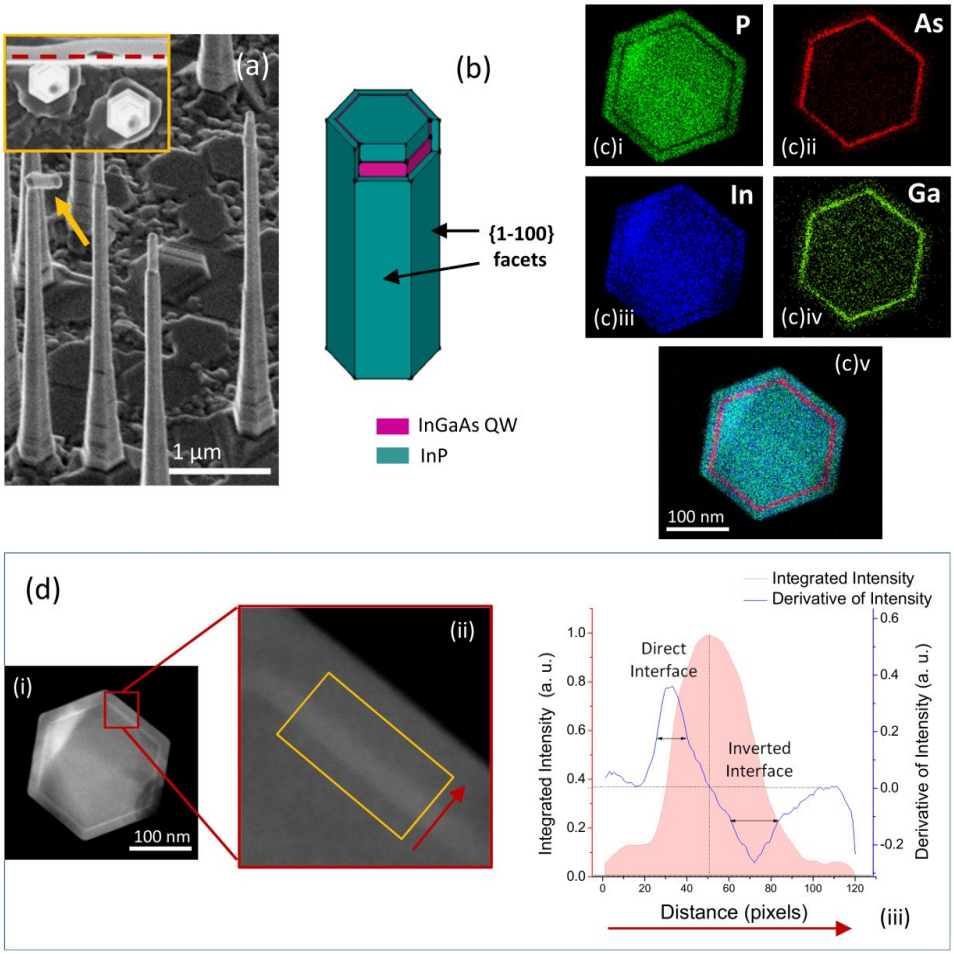

Fig. 1: Structural characterisation of the InP-$In_xGa_{1-x}As$ QW with 7 nm nominal thickness and $X_v = 0.55$. (a) 45° tilted SEM view of the whole QW structure; inset shows a top view of the same sample with respect to the cleavage edge marked in red. (b) Schematic of the nanowire QW indicating the {1-100} side facets. (c)i-iv elemental EDX maps of P, As, In and Ga, respectively, (c)v Overlay of all elemental maps shown in (c)i to iv. (d)i HAADF image of the same nanowire cross-section shown in (c), (d)ii The magnified view of the area marked in (d)i with the yellow box indicating the area used for the integrated intensity plot shown in (d)iii, and (d)iii Calculation of the direct and inverted interface sharpness using the derivative of the integrated intensity from the area shown by the yellow rectangle in (d)ii.

the As carryover effect,[35-37] and surface undulations and roughening that occur during the InGaAs growth and the subsequent growth interruption (before the second barrier growth)[31, 33, 34] are the more likely causes of the presently observed higher level of interdiffusion at the inverted interface, considering the current growth temperature and composition.

Fig. 2 (a) shows representative μ-PL spectrum taken from a single, nanowire QW at room temperature and another representative single nanowire spectrum taken at 77 K from the principal sample discussed in Fig. 1. The laser spot was focused on the middle of the nanowire. The nanowire QWs show bright emission with a clear single peak at room temperature as well as at 77 K. It should be noted that the ripples observed in the 1300 – 1400 nm range are due to system response and water vapour absorption. The two insets in Fig. 2 (a)i. and ii. are the magnified plots showing the 800 – 1000 nm wavelength range. It can be seen that no emission from the InP nanowire core or barrier is visible

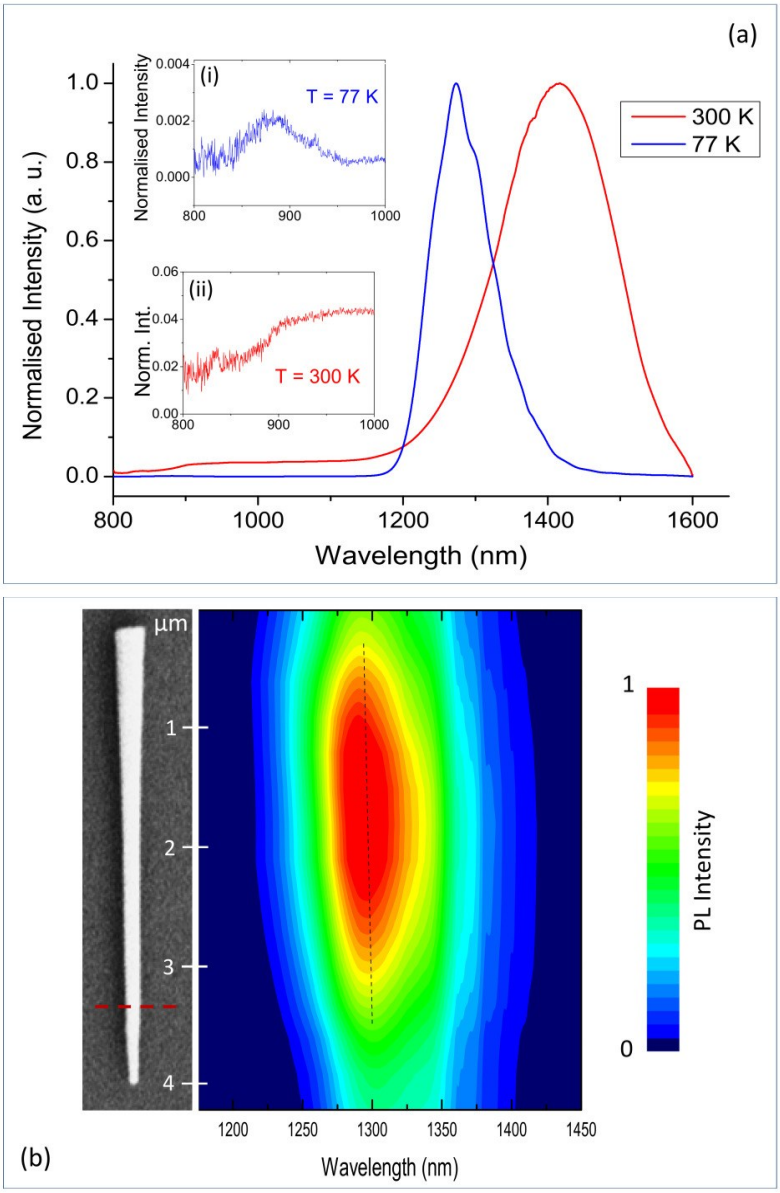

Fig. 2: Optical characterisation of single nanowire QWs. (a) Representative room temperature and 77 K μ-PL spectra from a single QW nanowire; insets (i) and (ii) zoom in to the 800-1000 nm wavelength region of the 77 and 300 K spectra, respectively, where InP emission is expected. (b) PL map of a single nanowire taken at 80 K; inset shows the SEM image of the nanowire scaled and rotated to align the PL map. Note that the tip of the nanowire is at the bottom part of the image.

at 300 K, whereas a very weak signal is observed at 77 K. This shows that the quantum well is highly efficient in capturing carriers, almost completely avoiding recombination in the InP core or outer barrier. This is one of the main differences and advantages of the current material system compared to the more commonly reported GaAs-AlGaAs nanowire QWs, where emission by the nanowire core is almost always visible and in most cases stronger than the GaAs QW emission[38-40] due to the presence of GaAs nanowire core, which has the lowest energy gap, hence forming the most preferred recombination location in the structure. The bright emission observed at room temperature and 77 K also indicates that there is no significant effect of the stacking faults observed along the nanowire on the PL efficiency.

μ-PL mapping was carried out in order to study the variation in emission along the long axis of the nanowire. Eight such maps were examined and Fig. 2 (b) shows a PL map from a representative nanowire with the SEM image of the same nanowire placed relative to the scan direction and y-axis of the map. Note that the intensity of PL from the top ~600 nm of the nanowire is much lower than the rest of the nanowire. The length of the InP nanowire core is ~3.6 μm as measured by SEM images of the InP nanowire core only growth and only this length would form the active region containing the QW. The top ~ 600 nm of the nanowire (marked by a red dashed line in Fig. 2 (b)) has grown during the InP outer barrier growth and would not contain the QW, and hence the expected lower PL intensity.

There is no or very little (< 18 nm) shift in emission peak along the length of the nanowire in all the nanowires measured. Rather broad linewidth observed in the single nanowire spectra (~ 166 nm) is also observed along the length of the nanowire in the map. This shows that the broadness in emission observed in the μ-PL spectra collected from the middle of the nanowire (Fig. 2 (a)) is not due to contributions from different areas of the nanowire that emit at different wavelengths, as it would have been if the QW thickness or composition varied along the nanowire.[11, 19] Instead, it suggests that it stems from a cause that is spatially shorter in range and common along the length of the nanowire. The rough inverted InGaAs-InP interface seen in Fig. 1 (d) could be the such most likely cause of this broadening. Alloy disorder and interface diffusion are also likely local causes considering the current alloy composition of InGaAs.[28, 41, 42] Monolayer fluctuations in QW thickness (especially those induced by the stacking faults),[18, 43, 44] band structure variation between WZ segments and stacking faults[45] and slight difference in QW thicknesses on different facets (caused by different levels of shadowing by the randomly placed neighbouring nanowires during growth)[46, 47] seen by X-TEM could also be reasons for the broad emission.

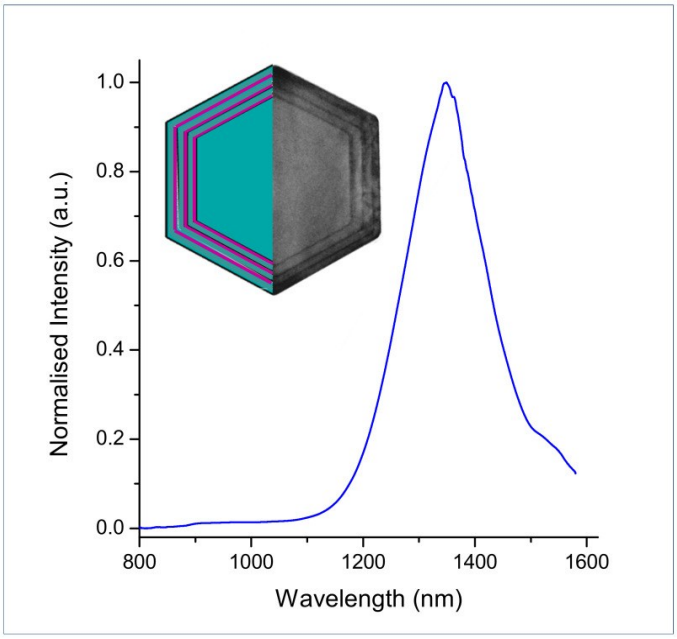

Fig. 3: A representative room temperature PL spectrum from a MQW single nanowire, inset shows an X-TEM image of a MQW NW aligned with a schematic.

MQWs, instead of SQWs are mostly used in optical communication related devices due to advantages such as higher efficiency, gain and total power output depending on the application and structure.[4, 6, 48] The SQW structure discussed so far was extended to grow three $In_{0.6}Ga_{0.4}As$ QWs separated by InP barriers. Fig. 3 shows the room temperature emission from a typical MQW nanowire with the inset showing a low magnification X-TEM image and the corresponding schematic. No excess broadening of emission was observed, contrary to the expected broader linewidth of MQWs.[48, 49] Although direct comparison of intensity may not be completely meaningful due to experimental errors in single nanowire measurements, it is seen that the MQW nanowires show higher emission intensity in general, with an average of approximately an order of magnitude higher intensity than that of the SQWs for the same excitation power.

The strong emission from the MQWs demonstrated here shows the scalability and the ability to extend the InP-InGaAs nanowire QWs to form more advanced structures with more QW active volume that could form the basis for devices such as lasers and LEDs.

3.2 Tunability of Emission Wavelength in Nanowire Single Quantum Wells

Tunability by Variation of Quantum Well Thickness

As mentioned earlier, one main advantage of ZB InP-InGaAs material combination is the possibility of avoiding lattice mismatch in heterostructure design by selecting the $In_xGa_{1-x}As$ composition to be x=0.53. In the case of QWs, this gives the opportunity to tune the QW emission almost in the complete wavelength range from bulk InP to bulk $In_{0.53}Ga_{0.47}As$ value without concerns on degradation of crystal quality or strain related complications, by changing the well thickness. A similar tunability of PL wavelength from 1420 nm to 1624 nm has been achieved by Takehiro *et al.* by increasing growth time of the $In_{0.53}Ga_{0.47}As$ shells from 10 to 60 s in InP-$In_{0.53}Ga_{0.47}As$-InP core-multi-shell nanowires.[25] However, it should be noted here, as shown in,[23] that complete axial and radial lattice matching between InP and $In_xGa_{1-x}As$ cannot be achieved in the WZ phase due to *a/c* ratio being different for the two materials (assuming Vegard's law). Nonetheless, minimal strain along *a* and/ or *c* axes can be obtained at values close to the above ZB value.[23]

In this work, the thickness of the WZ phase $In_{0.6}Ga_{0.4}As$ QWs is tuned to achieve emission wavelengths in the 1.3 – 1.55 μm region. Lattice mismatch of this composition with InP is small (only 0.51% and 0.37% along *a* and *c* axes, respectively). The well thickness was varied simply by changing the growth time from 20 to 180 s. The corresponding expected nominal thicknesses (calculated from available empirical data for the same reactor for the growth of ZB $In_{0.54}Ga_{0.46}As$ on InP (100) substrates) for these growth durations were 2 to 18 nm. The actual average thicknesses of the QWs were measured using high resolution (HR) TEM images of the nanowire cross-sections and are plotted against the growth time and nominal thickness in Fig. 4 (a). The QW thickness was measured using the derivative of the integrated intensity along the well as shown in Fig. 4 (b) in order to avoid ambiguity related to the diffused interfaces. QWs on the facets of at least five nanowires were measured for each data point.

The WZ QW growth rate on the nanowire facets is generally lower than nominal values expected from the empirical data for InGaAs growth on ZB InP (100) substrates, except in the case of very thin, 2 nm QW. This considerable difference is due to two reasons. First, the equivalent facet orientation of nanowires in the ZB phase itself is different from (100), and they generally grow slower than (100) facets under the considered growth conditions (for example {110} and {112} facets).[50 51] Second, the growth rate of the side facets of nanowires in WZ phase is inherently even lower than their ZB equivalent,[44, 52] making the actual thickness much lower than expected. However, the growth rate of the QWs seems to remain constant (when thicknesses > ~2 nm), showing a linear relationship for QW thickness with growth time.

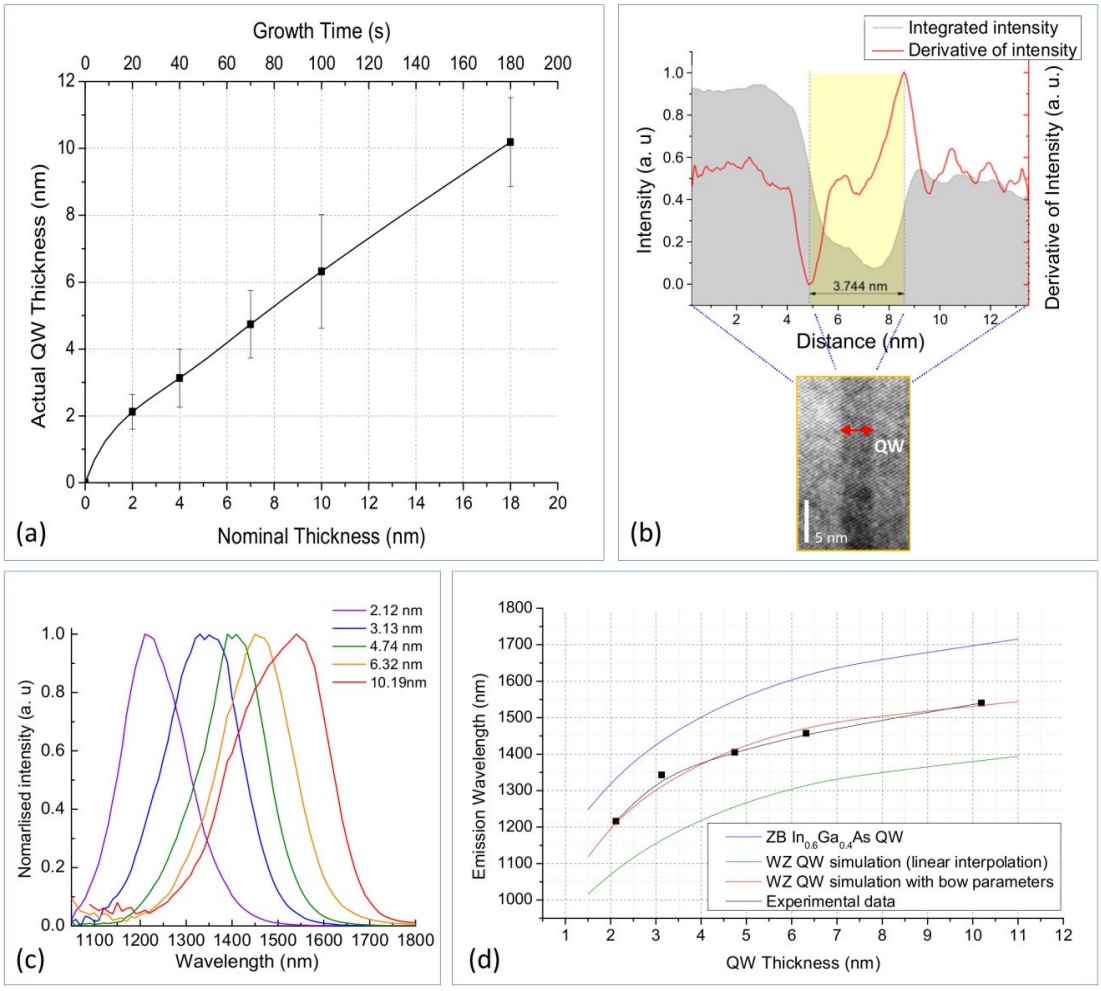

Fig. 4: Tunability of room temperature QW emission by varying thickness. (a) Actual thickness variation of the QW with the nominal thickness and growth time. Error bars represent the standard deviation of the measurements. (b) Calculation of actual QW thickness using the HR-TEM images. (c) PL spectra from ensembles of nanowires showing the monotonic red-shift in the emission wavelength with the increasing QW thickness. (d) Experimental and calculated emission wavelengths with and without bowing parameters as a function of QW thickness.

Fig. 4 (c) shows the monotonic shift in the room temperature emission wavelength with QW thickness in the 1.3 – 1.55 μm wavelength region. The black curve in Fig. 4 (d) plots the emission wavelength against actual QW thickness measured in Fig. 4 (a). The expected ground state emission wavelengths for $In_{0.6}Ga_{0.4}As$ QWs with thicknesses in the experimentally examined range were calculated using the single band effective mass approximation. The calculations were carried out for ZB phase (100) plane and WZ m-plane (the {1-100} family of planes – same as the facets of the nanowires) using the nextnano© simulation software.[53] Some of the key parameters used to create WZ phase InP and InGaAs materials are given in Table S1 in the Supporting Information. Arsenide and phosphide WZ materials are not available naturally in bulk form. Although, much research has been carried out and number of key parameters of the WZ phase materials have been experimentally determined,[26-28, 45, 54-59] it is still not possible to find all the material parameter values required for QW emission calculation in the literature. Therefore theoretically predicted values, ZB values, realistic estimations and linear interpolation are often used in most WZ calculations.[17, 18] Here too, the same approach is adopted where appropriate. The blue curve in Fig. 4 (d) shows variation of emission with thickness for ZB phase InP-$In_{0.6}Ga_{0.4}As$ QWs, while the green curve shows the same for the hexagonal WZ phase considering linear interpolation between GaAs and InAs values for all material parameters in order to calculate those of $In_{0.6}Ga_{0.4}As$. The valence and conduction band bowing parameters of InGaAs, which are two of the key parameters that is directly affecting the emission, was used as the fitting parameters in order to obtain the best fit (red) curve to the experimental values. The resulting valence and conduction band bowing parameters are -0.96 and -0.65 eV, respectively.

It could be seen that once the material system and the structure is modelled, together with the relationship between growth time and QW thickness given in Fig. 4 (a), they can be used to accurately and easily grow QWs with the required emission wavelength. In the next section, emission wavelength tuning in the 1.3 μm region by variation of QW composition is demonstrated.

Tunability by Variation of Quantum Well Composition

Despite many advantages, the approach of emission wavelength tuning by thickness variation could pose a few challenges, especially in the achievable high and low wavelength regions. The longest wavelength achievable is limited by the bulk band-gap of the chosen QW alloy and the sensitivity of the wavelength to thickness reduces for thicker QWs. In some cases, although not seen in the current study, relatively high level of broadening and multiple sharp peaks can be observed for very thin QWs due to higher sensitivity to mono-layer fluctuations and quantum dot-like formations.[18, 38, 39] Electron capture efficiency could also be low for very thin QWs. Varying emission wavelength by tuning the QW alloy composition minimises these limitations at very small and large thicknesses, albeit at the possible expense of formation of dislocations due to lattice mismatch. However, it should be noted that the possibility of dislocation formation is slightly less in the case of nanowire radial QWs compared to the planar case, due to the higher possibility of strain relaxation in the structure and

hence, even the composition range that can be accommodated is slightly larger than its planar counterpart of the same thickness.

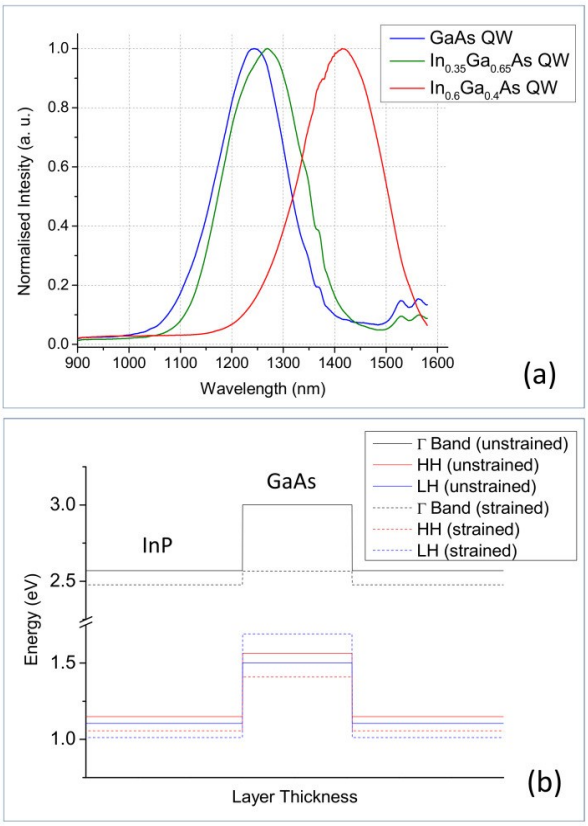

Fig. 5: Tunability of emission by varying QW composition. (a) Representative room temperature single nanowire PL spectra from GaAs, $In_{0.35}Ga_{0.65}As$ and $In_{0.6}Ga_{0.4}As$ QWs with a nominal thickness of 7 nm. (b) Band alignments between unstrained and strained WZ phase InP and GaAs.

Here, the composition of the QW is varied from GaAs to InAs. Fig. 5 (a) shows representative spectra from nominally 7 nm GaAs, $In_{0.35}Ga_{0.65}As$ and $In_{0.6}Ga_{0.4}As$ QWs. The spectra show a shift towards higher wavelengths with increasing In composition in the well, as expected. No reliable spectra could be obtained from the QWs with higher In composition ($X_v = 0.79$) or InAs QWs, most probably due to the emission being beyond the wavelength range of the InGaAs detector used. It should also be noted here, that even though the precursor flow rate and the growth time of the QWs were controlled in order to achieve QWs of same nominal thickness, due to the different growth rates of different compositions, the actual thickness from one composition to another could be different and hence the spectra may not be directly compared with each other.

One interesting observation is the QW-like behaviour of the GaAs insert. The band-gap of WZ GaAs is very close, but slightly higher than WZ InP with room temperature values of 1.437 and 1.421 eV

(863 and 872 nm), respectively.[54, 55] The lattice constant of GaAs on *m* (or *a*) planes is 3.5% smaller than InP (see Table S1)[26, 27] and hence, GaAs is under tensile strain. In the case of ZB, this strain shifts its band-gap below that of InP, forming a GaAs QW.[60, 61] Fig. 5 (b) shows the band alignments between unstrained WZ GaAs and InP as per Table S1 in Supplementary Information, and that between uniaxially strained WZ GaAs and InP, simulated similar to the discussion in Fig. 4 (d). It can be seen that formation of a GaAs QW in InP remains true in the case of WZ phase. In addition to strain and similar to the case of ZB,[60, 61] the band alignment between strained WZ GaAs and InP is type II. This contributes in further increasing the emission wavelength of the GaAs-InP QW and explaining the small difference observed between the peak positions of GaAs and $In_{0.35}Ga_{0.65}As$ QWTs.

Two approaches of emission wavelength tuning of InP-InGaAs nanowire QWs were presented in this section. Although each has some limitations, the two approaches together provides flexibility and control in tuning the emission of InP-InGaAs QWs grown on nanowires in the long distance optical communication wavelength range.

4. Conclusion:

This paper investigated the popular InP-InGaAs material combination which is commonly used in planar, telecommunications related device applications, in nanowire QW form. Single and multiple InGaAs radial QWs were grown on WZ phase InP nanowire cores and were capped with InP. The nanowire QWs were found to grow conformally around the nanowire core and showed some similarities to ZB phase planar InP-InGaAs QWs, such as interface diffusion and some dissimilarities such as broader PL. Despite this, optical characterisation revealed bright room temperature PL with strong carrier capture efficiency by the QW. Tunability of the QW emission was demonstrated in the 1.3 – 1.55 μm optical communications wavelength region by varying the QW thickness and in the 1.3 μm region by varying the $In_xGa_{1-x}As$ composition. The WZ InP-InGaAs QWs were optically modelled. This optical model and the knowledge of the growth rate of the QWs can be used to fine tune growth parameters in order to achieve the required wavelength values by tuning QW thickness. The results affirm the suitability of core-multi-shell InP-InGaAs nanowire QWs as building blocks for nanowire-based communication device applications. This work forms the basis to extend similar structures to include InGaAsP, further increasing the tunability, flexibility and scalability.

Acknowledgement:

The Australian authors acknowledge the Australian Research Council for the financial support. The Australian National Fabrication Facility and the Australian Microscopy and Microanalysis Research Facility are acknowledged for providing access to the equipment used. ASA would also like to thank the Malaysian Ministry of Education for her scholarship. DT, MDL and AP acknowledge funding by

Sapienza Università di Roma under the “Avvio alla Ricerca 2016” and “Avvio alla Ricerca 2015”, “Avvio alla Ricerca 2014”, and “Ateneo 2013” grants, respectively.

Conflicts of interest:

There are no conflicts of interest to declare.

Author Contributions:

PC and CJ conceptualised the experiments. HAF, PC and HHT grew the nanowires. HAF, ASA and YG carried out the TEM measurements. DT, HAF, MDL, FM, AP, ASA and FW performed various optical measurements. HAF, AP and ML carried out the simulations. HHT, AP and CJ supervised the entire project. HAF prepared the manuscript with input from all authors.

References

1. A. Stano, *Journal of The Electrochemical Society*, 1987, **134**, 448-452.
2. S. D. Gunapala, B. F. Levine, D. Ritter, R. Hamm and M. B. Panish, *Applied Physics Letters*, 1991, **58**, 2024-2026.
3. Y. Arslan, T. Colakoglu and C. Besikci, *Quantum Electronics, IEEE Journal of*, 2013, **49**, 186-195.
4. U. Koren, T. L. Koch, H. Presting and B. I. Miller, *Applied Physics Letters*, 1987, **50**, 368-370.
5. H. Uenohara, H. Iwamura and M. Naganuma, *Japanese Journal of Applied Physics*, 1990, **29**, L2442.
6. U. Koren, B. I. Miller, T. L. Koch, G. D. Boyd, R. J. Capik and C. E. Soccolich, *Applied Physics Letters*, 1986, **49**, 1602-1604.
7. K. C. Song, M. A. Matin, B. Robinson, J. G. Simmons, D. A. Thompson and P. Mascher, *Solid-State Electronics*, 1996, **39**, 1283-1287.
8. J. Zhang, M. A. Itzler, H. Zbinden and J.-W. Pan, *Light Sci Appl*, 2015, **4**, e286.
9. M. Heiss, Y. Fontana, A. Gustafsson, G. Wüst, C. Magen, D. D. O’Regan, J. W. Luo, B. Ketterer, S. Conesa-Boj, A. V. Kuhlmann, J. Houel, E. Russo-Averchi, J. R. Morante, M. Cantoni, N. Marzari, J. Arbiol, A. Zunger, R. J. Warburton and A. Fontcuberta i Morral, *Nat Mater*, 2013, **12**, 439-444.
10. F. Qian, Y. Li, S. Gradecak, H.-G. Park, Y. Dong, Y. Ding, Z. L. Wang and C. M. Lieber, *Nat Mater*, 2008, **7**, 701-706.
11. E. Dimakis, U. Jahn, M. Ramsteiner, A. Tahraoui, J. Grandal, X. Kong, O. Marquardt, A. Trampert, H. Riechert and L. Geelhaar, *Nano Letters*, 2014, **14**, 2604-2609.

12. K. Tomioka, M. Yoshimura and T. Fukui, *Nature*, 2012, **488**, 189-192.
13. C. Zheng, J. Wong-Leung, Q. Gao, H. H. Tan, C. Jagadish and J. Etheridge, *Nano Letters*, 2013, **13**, 3742-3748.
14. K. W. Ng, W. S. Ko, R. Chen, F. Lu, T.-T. D. Tran, K. Li and C. J. Chang-Hasnain, *ACS Applied Materials & Interfaces*, 2014, DOI: 10.1021/am503676c.
15. N. Sköld, J. B. Wagner, G. Karlsson, T. Hernán, W. Seifert, M.-E. Pistol and L. Samuelson, *Nano Letters*, 2006, **6**, 2743-2747.
16. M. E. Reimer, G. Bulgarini, N. Akopian, M. Hocevar, M. B. Bavinck, M. A. Verheijen, E. P. A. M. Bakkers, L. P. Kouwenhoven and V. Zwiller, *Nature Communications*, 2012, **3**, 737.
17. M. H. H. Alouane, R. Anufriev, N. Chauvin, H. Khmissi, K. Naji, B. Ilahi, H. Maaref, G. Patriarche, M. Gendry and C. Bru-Chevallier, *Nanotechnology*, 2011, **22**, 405702.
18. D. Lindgren, K. Kawaguchi, M. Heurlin, M. T. Borgström, M.-E. Pistol, L. Samuelson and A. Gustafsson, *Nanotechnology*, 2013, **24**, 225203.
19. S.-M. Ko, S.-H. Gong and Y.-H. Cho, *Nano Letters*, 2014, **14**, 4937-4942.
20. Z. Guoqiang, T. Kouta, B. Muhammad Danang, N. Masaya, S. Tetsuomi and G. Hideki, *Nanotechnology*, 2015, **26**, 115704.
21. D. M. Cornet and R. R. LaPierre, *Nanotechnology*, 2007, **18**, 385305.
22. B. Ganjipour, O. Tizno, M. Heurlin, M. T. Borgstrom, C. Thelander and L. Samuelson, 2014.
23. M. Heurlin, T. Stankevič, S. Mickevičius, S. Yngman, D. Lindgren, A. Mikkelsen, R. Feidenhans'l, M. T. Borgström and L. Samuelson, *Nano Letters*, 2015, **15**, 2462-2467.
24. F. Ren, K. W. Ng, K. Li, H. Sun and C. J. Chang-Hasnain, *Applied Physics Letters*, 2013, **102**, 012115.
25. O. Takehiro, A. Keita, T. Kohei, W. Takao and S. Kazuhiko, *Japanese Journal of Applied Physics*, 2016, **55**, 031201.
26. M. de la Mata, C. Magén, P. Caroff and J. Arbiol, *Nano Letters*, 2014, **14**, 6614-6620.
27. D. Kriegner, E. Wintersberger, K. Kawaguchi, J. Wallentin, M. T. Borgström and J. Stangl, *Nanotechnology*, 2011, **22**, 425704.
28. D. Kriegner, C. Panse, B. Mandl, K. A. Dick, M. Keplinger, J. M. Persson, P. Caroff, D. Ercolani, L. Sorba, F. Bechstedt, J. Stangl and G. Bauer, *Nano Letters*, 2011, **11**, 1483-1489.
29. Y.-N. Guo, T. Burgess, Q. Gao, H. H. Tan, C. Jagadish and J. Zou, *Nano Letters*, 2013, **13**, 5085-5089.
30. Y. Zhang, A. M. Sanchez, J. Wu, M. Aagesen, J. V. Holm, R. Beanland, T. Ward and H. Liu, *Nano Letters*, 2015, **15**, 3128-3133.
31. S. Juillaguet, R. Schwedler, A. Kohl, F. H. Baumann, B. Fraisse, J. Camassel, K. Wolter, K. Leo, B. Gallmann, M. Stollenwerck and J. P. Laurenti, 1993.
32. J. Decobert and G. Patriarche, *Journal of Applied Physics*, 2002, **92**, 5749-5755.

33. G. Patriarche, F. Glas, G. Le Roux, L. Largeau, A. Mereuta, A. Ougazzaden and J. L. Benchimol, *Journal of Crystal Growth*, 2000, **221**, 12-19.
34. I. Yamakawa, R. Oga, Y. Fujiwara, Y. Takeda and A. Nakamura, *Applied Physics Letters*, 2004, **84**, 4436-4438.
35. A. R. Clawson, X. Jiang, P. K. L. Yu, C. M. Hanson and T. T. Vu, *JEM*, 1993, **22**, 155-160.
36. X. S. Jiang, A. R. Clawson and P. K. L. Yu, *Journal of Crystal Growth*, 1995, **147**, 8-12.
37. C. Huajie, R. M. Feenstra, P. G. Piva, R. D. Goldberg, I. V. Mitchell, G. C. Aers, P. J. Poole and S. Charbonneau, *Applied Physics Letters*, 1999, **75**, 79-81.
38. M. Fickenscher, T. Shi, H. E. Jackson, L. M. Smith, J. M. Yarrison-Rice, C. Zheng, P. Miller, J. Etheridge, B. M. Wong, Q. Gao, S. Deshpande, H. H. Tan and C. Jagadish, *Nano Letters*, 2013, **13**, 1016-1022.
39. D. Spirkoska, G. Abstreiter and A. F. i. Morral, *Semiconductor Science and Technology*, 2009, **24**, 113001.
40. M. Heigoldt, J. Arbiol, D. Spirkoska, J. M. Rebled, S. Conesa-Boj, G. Abstreiter, F. Peiro, J. R. Morante and A. Fontcuberta i Morral, *Journal of Materials Chemistry*, 2009, **19**, 840-848.
41. E. F. Schubert and W. T. Tsang, *Physical Review B*, 1986, **34**, 2991-2994.
42. R. Zimmermann, *Journal of Crystal Growth*, 1990, **101**, 346-349.
43. P. J. Poole, D. Dalacu, X. Wu, J. Lapointe and K. Mnaymneh, *Nanotechnology*, 2012, **23**, 385205.
44. S. G. Ghalamestani, M. Heurlin, L.-E. Wernersson, S. Lehmann and K. A. Dick, *Nanotechnology*, 2012, **23**, 285601.
45. K. Pemasiri, M. Montazeri, R. Gass, L. M. Smith, H. E. Jackson, J. Yarrison-Rice, S. Paiman, Q. Gao, H. H. Tan, C. Jagadish, X. Zhang and J. Zou, *Nano Letters*, 2009, **9**, 648-654.
46. A. Kelrich, Y. Calahorra, Y. Greenberg, A. Gavrilov, S. Cohen and D. Ritter, *Nanotechnology*, 2013, **24**, 475302.
47. N. V. Sibirev, M. Tchernycheva, M. A. Timofeeva, J.-C. Harmand, G. E. Cirlin and V. G. Dubrovskii, *Journal of Applied Physics*, 2012, **111**, 104317.
48. Y. Arakawa and A. Yariv, *Quantum Electronics, IEEE Journal of*, 1986, **22**, 1887-1899.
49. Y. Arakawa and A. Yariv, *Quantum Electronics, IEEE Journal of*, 1985, **21**, 1666-1674.
50. S. H. Jones, L. K. Seidel, K. M. Lau and M. Harold, *Journal of Crystal Growth*, 1991, **108**, 73-88.
51. O. Kayser, *Journal of Crystal Growth*, 1991, **107**, 989-998.
52. S. Lehmann, J. Wallentin, D. Jacobsson, K. Deppert and K. A. Dick, *Nano Letters*, 2013, **13**, 4099-4105.
53. http://www.nextnano.com/ Last accessed: 16/10/2016).

54. M. De Luca, G. Lavenuta, A. Polimeni, S. Rubini, V. Grillo, F. Mura, A. Miriametro, M. Capizzi and F. Martelli, *Physical Review B*, 2013, **87**, 235304.

55. A. Zilli, M. De Luca, D. Tedeschi, H. A. Fonseka, A. Miriametro, H. H. Tan, C. Jagadish, M. Capizzi and A. Polimeni, *ACS Nano*, 2015, DOI: 10.1021/acsnano.5b00699.

56. M. B. Rota, A. S. Ameruddin, H. A. Fonseka, Q. Gao, F. Mura, A. Polimeni, A. Miriametro, H. H. Tan, C. Jagadish and M. Capizzi, *Nano Letters*, 2016, **16**, 5197-5203.

57. M. W. Larsson, J. B. Wagner, M. Wallin, P. Håkansson, L. E. Fröberg, L. Samuelson and L. R. Wallenberg, *Nanotechnology*, 2006, **18**, 015504.

58. J. K. Panda, A. Chakraborty, D. Ercolani, M. Gemmi, L. Sorba and A. Roy, *Nanotechnology*, 2016, **27**, 415201.

59. N. Vainorius, D. Jacobsson, S. Lehmann, A. Gustafsson, K. A. Dick, L. Samuelson and M.-E. Pistol, *Physical Review B*, 2014, **89**, 165423.

60. D. Gershoni, H. Temkin, J. Vandenberg, S. Chu, R. Hamm and M. Panish, *Physical Review Letters*, 1988, **60**, 448-451.

61. M. E. Pistol, M. Gerling, D. Hessman and L. Samuelson, *Physical Review B*, 1992, **45**, 3628-3635.